New Journal of Physics
The open access journal at the forefront of physics

Deutsche Physikalische Gesellschaft DPG IOP Institute of Physics

PAPER • OPEN ACCESS

Transients and multiperiodic responses: a hierarchy of material bits

To cite this article: Colin M Meulblok and Martin van Hecke 2026 *New J. Phys.* **28** 025002

IOP Publishing New J. Phys. 28 (2026) 025002 https://doi.org/10.1088/1367-2630/ae45c7

New Journal of Physics
The open access journal at the forefront of physics

Deutsche Physikalische Gesellschaft DPG
IOP Institute of Physics

Published in partnership with: Deutsche Physikalische Gesellschaft and the Institute of Physics

OPEN ACCESS

RECEIVED
8 October 2025

REVISED
2 February 2026

ACCEPTED FOR PUBLICATION
13 February 2026

PUBLISHED
23 February 2026

PAPER

Transients and multiperiodic responses: a hierarchy of material bits

Colin M Meulblok[1,2,*] **and Martin van Hecke**[1,2]

[1] AMOLF, Amsterdam, The Netherlands
[2] LION, Leiden University, Leiden, The Netherlands
[*] Author to whom any correspondence should be addressed.

E-mail: meulblok@physics.leidenuniv.nl

Keywords: memory, multiperiodic orbits, mechanical metamaterials

Supplementary material for this article is available online

Abstract

When cyclically driven, certain disordered materials exhibit transient and multiperiodic responses that are difficult to reproduce in synthetic materials. Here, we show that elementary multiperiodic elements with period $T = 2$ — togglerons—can serve as building blocks for such responses. We experimentally realize metamaterials composed of togglerons with tunable transients and periodic responses-including odd periods. Our approach suggests a hierarchy of increasingly complex elements in frustrated media, and opens a new strategy for rational design of sequential metamaterials.

1. Introduction

The sequential response of frustrated materials to cyclic driving reveals a wide range of memory effects [1–10]. These memory effects range from return-point memory, where extrema of cyclic driving sweeps are encoded in the material and can be detected as kinks in the response function [10–13], to more complex memory effects where, e.g. the material responds to the number of identical driving cycles [7–10, 14–17]. Understanding the emergence and organization of these memory effects provides key insight into the complex physics of disordered systems and the structure of their underlying energy landscapes [13, 18]. Moreover, reproducing such sequential responses in designer materials enables the realization of sequential shape morphing [19–25], adaptive mechanical behavior [26], and *in-materia* computing such a counting of periodic signals or filtering specific driving sequences [15, 16, 27–32].

At zero temperature and in the absence of plastic evolution, even massively multistable systems with a large number of states inevitably evolve toward a repeating pattern under purely cyclic, periodic driving [7, 15, 33–41]. The complete evolution of such a system is referred to as an *orbit*, which is the sequence of states under a specific driving protocol (figure 1(a)). For cyclic driving, orbits eventually repeat periodically. This allows defining the *transient* τ as the number of driving cycles required to reach a periodic response, and the *period* T as the number of driving cycles needed to complete one repetition of that response. Together, τ and T serve as fundamental descriptors of the material's sequential response under cyclic driving. Recently, non-trivial finite transients have been observed in metamaterials and simplified crumpled sheets [15, 16], whereas *multiperiodic* responses with $T > 0$ have been seen in a wide variety of simulations [7, 10, 15, 33–41]. Understanding and controlling such transients and multiperiodic responses gives insight into the rich physics of frustrated materials and, when harnessed through rational design, opens routes to smart materials with advanced sequential functionalities [16, 24, 28, 29, 42].

To facilitate the analysis and modeling of frustrated materials under cyclic drive, these systems can be described as collections of interacting multi-state elements, with binary spins and hysterons popular choices [6, 7, 13, 18, 39–41, 43–46]. For isolated spins, their internal state or phase is solely determined by whether the instantaneous value of the driving parameter ε is smaller or larger than a

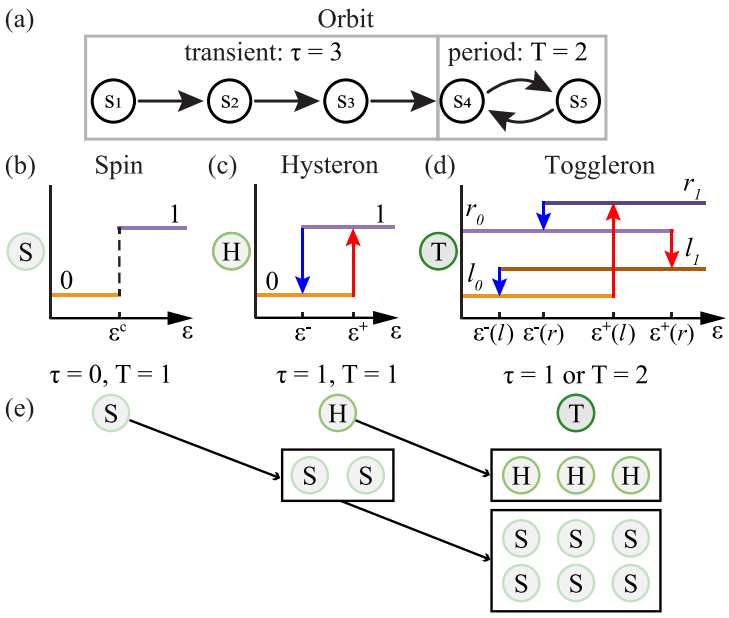

Figure 1. Orbits and material bits. (a) An example orbit under cyclic driving, evolving through five states $\{s_1, \ldots, s_5\}$ with transient $\tau = 3$ and period $T = 2$. Each circle represents a state and each directed edge a single drive cycle. (b)–(d) Transitions and switching thresholds for spins, hysterons and togglerons. Even though togglerons have more than two states, we refer to these as material bits. (e) Hierarchy of material bits: two interacting spins (S) can model a hysteron (H); six interacting spins or three interacting hysterons can model a toggleron (T).

critical threshold value (figure 1(b)). In contrast, hysterons retain memory of past driving, and their phase is governed by both the current value and history of ε (figure 1(c)). We note that pairs of spins with appropriately chosen interactions can capture the hysteretic response of a single hysteron (see appendix A). Hence, we view spins and hysterons as the lowest ranks in a hierarchy of increasingly complex elements, where elements of higher rank can be realized by combining multiple interacting elements of a lower rank (figure 1(e)).

Interactions between these elements are essential for producing nontrival transients and multiperiodic behavior; for example, $T = 2$ orbits require six interacting spins or three interacting hysterons [14, 39] (figure 1(e); see appendix A). Hence, longer transients or periods require a larger number of interacting elements to be modeled. The growing dimensionality of the associated parameter space makes it increasingly difficult to navigate this space. Moreover, this makes designing and understanding long-period responses challenging. This challenge motivates an exploration of the trade-off between the complexity of individual elements and the number of elements required to achieve specific behaviors and orbits (figures 1(b)–(e)).

Here we introduce *togglerons*, elements that return to their initial state after two driving cycles, as effective building blocks to understand and realize both transient and multiperiodic behavior (figure 1(d)). Spins, hysterons and togglerons are part of a hierarchy, where elements of higher rank mimic multiple interacting elements of a lower rank; not only can two interacting spins form a single hysteron, togglerons can be formed from groups of spins or hysterons (figure 1(e); see appendix A). Such a hierarchical perspective naturally captures the balance between the complexity of each elements and the number required for specific orbits, and suggests that studying higher-order responses through more complex building blocks–such as period-two units–offers a promising route toward understanding the origin of longer periods and designing metamaterials with programmable sequential dynamics.

We focus on mechanical togglerons and materialize these with cyclically compressed beams that buckle in a constrained environment. We investigate interacting togglerons and show how to design their properties and interactions to realize targeted orbits. We finally materialize a toggleron-metamaterial which, depending on the amplitude of the cyclic drive, exhibits orbits with $(\tau, T) = (2, 2), (0, 4)$ or $(1, 3)$. Our hierarchical framework, where clusters of simple interacting elements form aggregate units with complex sequential responses, enables the design of smart materials for sensing, soft robotics, and sequential *in materia* computing.

2. Results and discussion

2.1. Togglerons

We introduce a *toggleron*, a single element that exhibits an intrinsic period-two response under cyclic driving. Its orbit consists of four distinct states connected by four irreversible transitions (figure 1(d)). Specifically, the toggleron undergoes one irreversible transition during each increase and decrease of the driving field, and returns to its initial state only after two full driving cycles.

To clarify the relation to hysterons, we label these states l_0, l_1, r_0 and r_1 (figures 1(b)–(d)). The subscript '0' and '1' denotes stability at low and high values of the driving field, respectively, while the labels l (left) and r (right) distinguish two symmetry-related states. The transition from the '0' to '1' states occur during increasing drive, while transitions from the '1' to '0' states occur during decreasing drive. In contrast, the transitions between l and r states occur only during increasing drive [3] (figure 1(d)). Thus, the usual hysteron states '0' (low) and '1' (high) are effectively doubled into left and right flavors; a toggleron cannot be reduced to a single bistable unit (figures 1(b) and (c)).

Over the course of two driving cycles, a toggleron follows a specific transition sequence: during the first up-sweep of the driving field ε, it switches from configuration l_0–r_1 at switching threshold $\varepsilon^+(l)$. On the subsequent down-sweep, it transitions from r_1 to r_0 at $\varepsilon^-(r)$. In the next cycle, the configuration evolves from $r_0 \uparrow l_1 \downarrow l_0$, with switching events at $\varepsilon^+(r)$ and $\varepsilon^-(l)$, respectively (figure 1(d)).

The $T = 2$ behavior requires that both down switching thresholds ε^- are smaller than both up switching thresholds ε^+, and that the cyclic protocol is chosen so that the driving passes through all thresholds $\varepsilon^\pm$ [47]. Importantly, multiperiodicity arises within a *single* element and does not rely on interactions between multiple hysterons or spins with finely tuned coupling strengths (figures 1(b)–(d), see appendix A).

We materialize mechanical togglerons using slender beams ($L_0 = 100$ mm) constrained by lateral boundaries with two protrusions, or tips [48]. Under cyclic compression of the beam, these tips induce snapping between its left- and right-buckled configurations. We non-dimensionalize all lengths by L_0, including the width t and center position x_b of the beam. The lateral boundaries are fixed to the bottom plate, and are parameterized by their heights z_b and z_t and horizontal position x_l and x_r (figure 2(a); see appendix B). The system is driven by quasistatic compression cycles, with strain ε varying between the minimal value ε_m and a maximum value ε_M. Crucially, we take $\varepsilon_m > \varepsilon_b$, where ε_b is the buckling strain, which ensures that the beam remains buckled and history dependent [15].

To demonstrate the targeted sequential evolution, a toggleron is initialized in the left-buckled configuration l_0 and its beam's mid-point deflection x_b is tracked as the compression ε is cycled (figures 2(b) and (c), see movie 1). The toggleron exhibits a reproducible sequence of configurations, undergoing four distinct irreversible transitions over two cycles–one during each up or down sweep of ε–and returns to its initial configuration at the end of the second cycle, as required (figure 2(b), see movie 1).

To examine the sequence of configurations in more detail, we present snapshots of the real-space configuration immediately before and after each irreversible transitions (figure 2(b)), together with the full evolution of the mid-point x_b (figure 2(c)). During increasing ε, transitions between left-buckled l and right-buckled r configurations are triggered by the buckled beam coming into contact with the lateral tips (figure 2(b-i)). This contact constrains the deformation and initially induces a smooth evolution into a higher-order buckling mode without loss of stability (figures 2(b-ii) and (c)). Upon further increase of ε, this constrained configuration loses stability, resulting in an irreversible snapping event in which the beam transitions to a right-leaning configuration r_1 (figure 2(b-iii)).

Under decreasing ε, the beam again initially deforms smoothly (figures 2(b-iv) and (c)) before undergoing a (subtle) unsnapping transition (figure 2(b-v)). Although this unsnapping event involves only a small jump of x_b (figure 2(c), inset), it is irreversible–under subsequent compression, the configurations r_1 and r_0 (and analogously l_1 and l_1) evolve along qualitatively different branches of the $x_b(\varepsilon)$ response (figures 1(d) and 2(c), see appendix B).

The rationale for the use of dual-tip boundaries is as follows [48]. To allow lateral deflection of the beam, the tips of the left and right boundaries must be placed to the left ($x_l < 0$) and right ($x_r > 0$) of the beam. Yet, these boundaries must induce snapping of the beam. Specifically, if a beam is initially buckled to the left, increasing compression should trigger a snap-through transition to the right. However, for a boundary with a single tip, compression induced snapping from left to right is impossible, since it requires $x_l > 0$ [30, 48–50]. In contrast, the dual-tip geometry allows to exert a

[3] Other realizations where, e.g. such transitions occur under decreasing driving can be mapped to our representation by relabeling of the states.

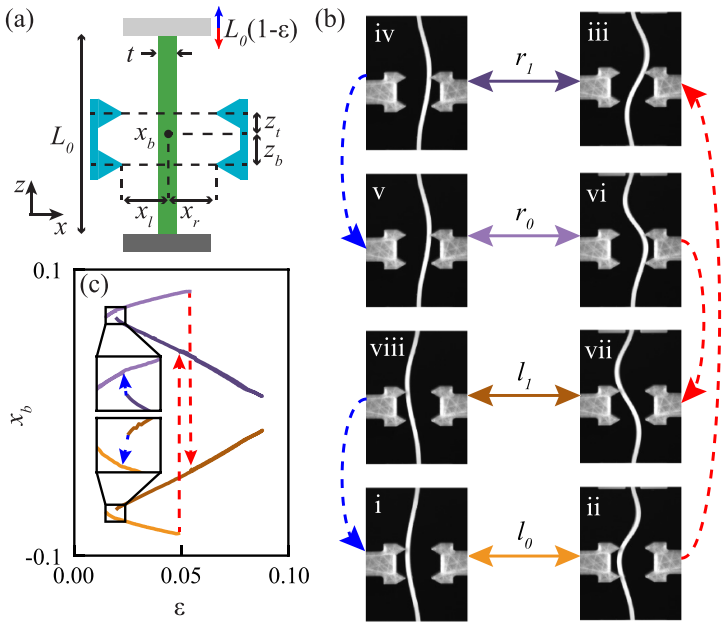

Figure 2. Geometry and phenomenology of togglerons. (a) We realize togglerons using a slender beam (green) constrained by fixed lateral boundaries consisting of dual tips (blue). The black circle at the center of the beam at rest indicates the origin of the (x, z) coordinate frame. (b)–(c) Evolution of a toggleron during two compression cycles ($(\varepsilon_m, \varepsilon_M) = (0.015, 0.088)$, $(t, z_t, z_b, x_l, x_r) = (0.025, 0.02, -0.16, -0.08, 0.08)$. Snapshots (b) show the beam configuration immediately before and after the irreversible transitions (dashed) during compression (red) and decompression (blue). Bidirectional arrows indicate reversible beam evolution and show the four states r_1, r_0, l_1 and l_0; colors match the four stable branches of the mid-point deflection x_b shown in panel (c). Irreversible transitions occur rapidly, effectively at fixed ε, and are indicated by (vertical) dashed arrows. (c) Evolution of x_b; smooth evolution of the configuration within a given state are shown as colored curves, and the irreversible transitions as red and blue arrows. Insets highlight the irreversible transitions at $\varepsilon^-(0)$ and $\varepsilon^-(1)$. .

moment on the beam, and when properly designed, induces snapping from l to r for $x_l < 0$, thus powering the toggling motion of the beam [48].

The locations of the tips directly control the critical thresholds. A wide range of vertical positions z_b, z_t induces snapping, and increasing the lateral distance between the tips and the beam—i.e. increasing $|x_l|$ or x_r—raises $\varepsilon^+(l)$ and $\varepsilon^+(r)$ [48]. In the example above, the toggleron is left-right symmetry ($x_l = -x_r$) so that $\varepsilon^+(l) = \varepsilon^+(r)$ and $\varepsilon^-(l) = \varepsilon^-(r)$. Breaking this symmetry–by introducing a difference between the horizontal positions x_l, x_r, or introducing differences between the vertical positions of left and right tips—allows for independent control over $\varepsilon^\pm(l)$ and $\varepsilon^\pm(r)$. Hence, the dual-tip design robustly and controllably produces toggling behavior over a broad range of geometric parameters (for more details see [48]).

Togglerons exhibit both multiperiodic and transient behavior. Consider periodic driving of (asymmetric) togglerons for $\varepsilon_m < \varepsilon^-$ so that the $l_1 \to l_0$ and $r_1 \to r_0$ transitions always occur. The (relative) values of $\varepsilon^+(l), \varepsilon^+(r)$ and ε_M then control the evolution after each full driving cycle, allowing to drop the '0' and '1' indices and to characterize the toggleron as l or r. When $\varepsilon_M < \varepsilon^+(l)$ and $\varepsilon_M < \varepsilon^+(r)$, the toggleron remains stuck and $(\tau, T) = (0, 1)$. When ε_M exceeds both switching thresholds, $(\tau, T) = (0, 2)$. For $\varepsilon^+(l) < \varepsilon_M < \varepsilon^+(r)$, which can be realized by taking $|x_l| < |x_r|$, the evolution depends on the initial state: Starting from r, the toggleron remains stuck, while starting from l, it first evolves to r and then remains stuck, leading to an elementary transient: $(\tau, T) = (1, 1)$.

2.2. Interactions and complex orbits

To explore a broader range of transients and multiperiodic orbits [15, 33–41], we consider two interacting togglerons. We denote their collective states as $S = (ll), (lr), (rl)$ or (rr), and note that these four states constrain the possible transients and periods to $\tau + T \leqslant 4$. We encode interactions in eight the state-dependent switching thresholds $\varepsilon_i^+(S)$, where $i = 1, 2$ labels the toggleron.

The language of finite state machines is useful to describe the response of multistable systems to sequential driving [16]. Finite state machines (FSMs) consist of a (finite) collection of states and input characters, and are defined by the transition table which specifies how an input character advances the machine from state to state [51, 52]. The collective states of a (finite) interacting toggleron system thus form the states of the corresponding FSM. To discretize the input, we note that the physical thresholds partition ε into nine intervals—we assume that the thresholds are non-degenerate - and

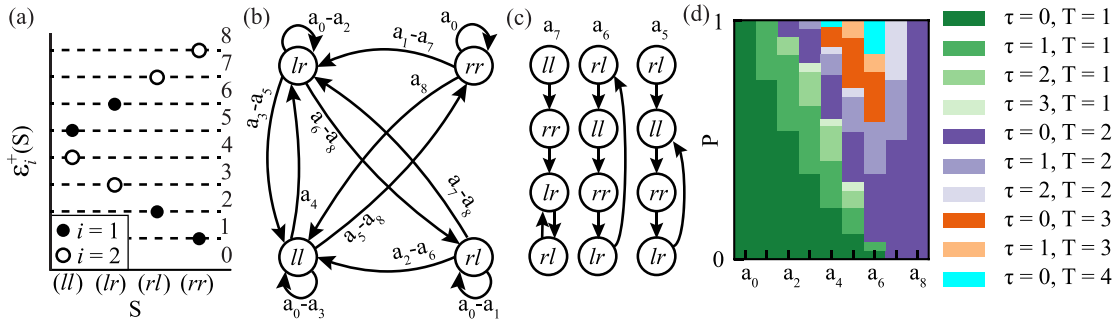

Figure 3. Evolution of two interacting togglerons. (a) Example of the ordering of the eight switching thresholds $\varepsilon_i^+(S)$ (symbols) which define nine strain intervals (0–8). (b) Corresponding FSM diagram. (c) Three example orbits under cyclic driving with a_7, a_6, and a_5. (d) Normalized stacked bar chart for (τ, T).

that the response to a single driving cycle $\varepsilon : \varepsilon_m \uparrow \varepsilon_M \downarrow \varepsilon_m$ depends only on the interval containing the maximal driving value ε_M (figure 3(a)) [16, 45]. We choose one representative value ε_M^k in each interval $k = 0, 1, \ldots, 8$ and define nine input characters a_k representing full driving cycles $\varepsilon : \varepsilon_m \uparrow \varepsilon_M^k \downarrow \varepsilon_m$ (figure 3(a)) [16]. Together, this allows to determine the evolution of any initial state S_0 after one driving cycle, $S_1 = a_k(S_0)$, thereby defining the transition table and enabling a graphical representation of the resulting FSM (figure 3(b)) [16].

Different orderings of the thresholds lead to different FSMs. We experimentally explored several orderings and verified that the FSM framework describes all cases; numerically we have explored all 8! ($\approx 4 \cdot 10^4$) possible orderings of the thresholds (see below). We believe that our physical design parameters are sufficiently diverse to realize a substantial fraction if not all orderings that respect that all up thresholds are larger than all down thresholds. Crucially, we realized the specific ordering shown in figure 3(a) that allows to vary τ and T by the maximal compression of the cyclic driving.

The FSM facilitates classification of transients and multiperiodic responses under cyclic driving. For example, for $\varepsilon_M = \varepsilon_M^7$, the response can be tracked by following the transitions in the FSM under repeated compression cycles a_7. Starting from $S_0 = (ll)$, the system exhibits a transient of two before entering an orbit with $T = 2$: $(ll) \xrightarrow{a_7} (rr) \xrightarrow{a_7} (lr) \xrightarrow{a_7} (rl) \xrightarrow{a_7} (lr) \xrightarrow{a_7} \ldots$ (figures 3(b) and (c)). Other initial states yield $(\tau = 1, T = 2)$ and $(\tau = 0, T = 2)$. Similarly, for $\varepsilon_M = \varepsilon_M^6$, a cycle of maximal length four $(\tau = 0, T = 4)$ is observed. Strikingly, for $\varepsilon_M = \varepsilon_M^7$, a cycle of period *three* emerges (figure 3(c)).

Since the possible transients and periods only depend on the ordering of these thresholds, we determine (τ, T) for all 8! orderings and explore their statistics (figure 3(d)). The combination of non-symmetric elements ($\varepsilon^+(l) \neq \varepsilon^+(r)$) and interactions enables the realization of all allowed combinations of τ and T, including multiperiodic orbits with odd periods. Together, our data and examples illustrate that interacting togglerons exhibit a wide range of transients and multiperiodic orbits which depend on driving amplitude and initial state.

2.3. Design of orbits

For each orbit, conditions on the ordering of the switching thresholds can straightforwardly be designed. We illustrate this for the orbit $(rl) \xrightarrow{a_k} (ll) \xrightarrow{a_k} (rr) \xrightarrow{a_k} (lr) \xrightarrow{a_k} (ll) \xrightarrow{a_k} \ldots$. Each transition, e.g. $(rl) \xrightarrow{a_k} (ll)$ produces two design inequalities, i.e. $\varepsilon_1^+(rl) < \varepsilon_M^k$ and $\varepsilon_2^+(rl) > \varepsilon_M^k$. These transitions collectively impose up to eight inequalities and define one or more admissible orderings of the switching thresholds and associated ranges for ε_M. Note that for the specific design problem of finding switching thresholds that exhibit the three orbits shown in figure 3(c), we only require the specific ordering of the four largest thresholds, i.e. a partial order of the thresholds [45]. Hence, specific (combinations of) orbits, transients and periods can be designed by controlling the switching thresholds.

This simple design strategy highlights the utility of togglerons. Realizing similar orbits with spins and hysterons require solving a larger, more intricate set of design inequalities [16, 17, 39, 44, 45]. This is primarily due to their limited response in isolation—hysterons can exhibit at most a $\tau = 1$ response, while spins lack any transient behavior. By employing a more versatile unit such as a toggleron, which can exhibit both multiperiodic and transient responses, the design of more complex orbits becomes markedly more straightforward.

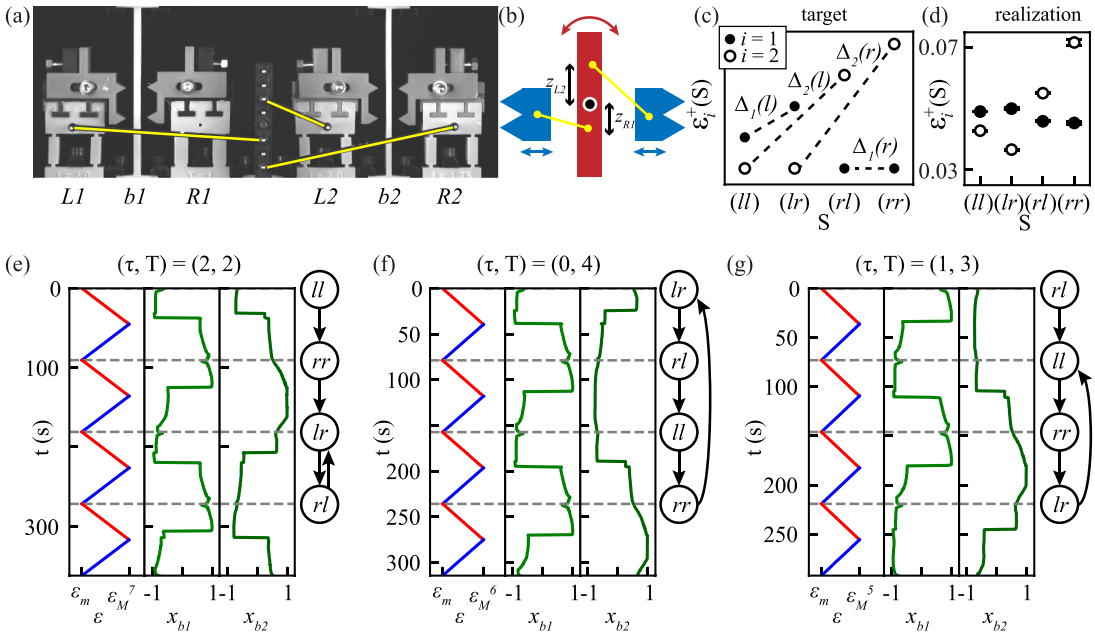

Figure 4. Metamaterial consisting of two interacting togglerons. (a) Geometry highlighting the connections from the flexible boundaries L_1, L_2 and R_2 to a central rotating arm (yellow; see appendix (B). (b) Schematic representation of the coupling between boundaries L_2 and R_1. (c) Target ordering of the switching thresholds. (d) Realized switching thresholds for our specific design (for our specific design, see appendix (B). Error bars are included but are smaller than the marker size and therefore not clearly visible. The measured bare thresholds are $(e_1^+(l), e_1^+(r), e_2^+(l), e_2^+(r)) = (0.051, 0.44, 0.50, 0.53)$ and the interactions are $(\Delta_1^+(l), \Delta_1^+(r), \Delta_2^+(l), \Delta_2^+(r)) = (0.00, 0.001, 0.005, 0.019)$. (e)–(g) Evolution of the mid-point deflections x_{b_1} and x_{b_2} during four compression cycles with amplitude $\varepsilon_M^7 = 0.056$, $\varepsilon_M^6 = 0.050$, and $\varepsilon_M^5 = 0.047$, showing orbits with $\{\tau, T\} = \{2,2\}$, $\{0,4\}$ and $\{1,3\}$.

2.4. Materializing target orbits

To demonstrate the feasibility of this approach, we create a metamaterial that realizes the three orbits shown in figure 3(c). This metamaterial consists of two asymmetric, interacting togglerons, where flexible lateral boundaries mediate their interactions (figure 4(a)). We control the left-right symmetry by the spacing (at rest) between beam and boundaries (L_i, R_i) (figures 4(a) and (b)). Interactions are implemented by placing the lateral boundaries on a weakly deformable structure. Hence, when, e.g. beam one is in contact with its right pusher it displaces it, and by coupling the right pusher of beam one with, e.g. the left pusher of beam two, interactions between the togglerons are realized.

We couple the boundaries via a rotating structure, which allows independent control over the magnitude and sign of the interactions (figure 4(b)). The sign is determined by the connection of the rotating structure. For example, when the right pusher of beam one and the left pusher of beam two are connected on opposite sides of the center of rotation, the pushers move outward relative to their respective beam, inducing a negative interaction. In contrast, when both pushers are connected on the same side of the center of rotation, the outward movement of one results in an inward movement of the other, resulting in a positive interaction. The magnitude is controlled by the lever arm of the rotating structure and by the stiffness of the pushers (figure 4(b)). Together, these design parameters allow systematic tuning of both the strength and sign of the coupling between togglerons.

Materializing the target orbits requires a partial order of the thresholds, where the four largest thresholds are $\varepsilon_1^+(ll) < \varepsilon_1^+(lr) < \varepsilon_2^+(rl) < \varepsilon_2^+(rr)$ (figure 4(c)). The differences between, e.g. $\varepsilon_1^+(ll)$ and $\varepsilon_1^+(lr)$ (dashed lines in figure 4(c) necessitate interactions between the togglerons, which we model as

$$\varepsilon_i^+(S) = e_i^+(s_i) + \Delta_i(s_i)\, B\left(s_j\right). \tag{1}$$

Here $B(l) := -1$, $B(r) := 1$, and $e_1^+(l)$, $e_1^+(r)$, $e_2^+(l)$ and $e_2^+(r)$ denote the 'bare' thresholds of the isolated togglerons. The interaction strengths are given by $\Delta_i(s_i)$, where, e.g. $\Delta_1(l) := (\varepsilon_1^+(lr) - \varepsilon_1^+(ll))/2$ denotes how strong toggleron two modifies the threshold of phase l of toggleron one. Hence, the targeted ordering implies three conditions: *(i)* $\Delta_1(r) \approx 0$; *(ii)* $\Delta_1(l) > 0, \Delta_2(l) > 0$ and $\Delta_2(r) > 0$; *(iii)* $\Delta_1(l) \ll \Delta_2(l) < \Delta_2(r)$ (figure 4(c)).

We implement these conditions by selecting appropriate design parameters. First, condition *(i)* is satisfied by boundary R_1 being uncoupled from other boundaries. Second, the sign of the interactions (condition *(ii)*) implies that the coupling makes boundaries L_1, L_2 and R_1 all move in and outward together, which requires that $z_{L_1}/z_{R_2} > 0$ and $z_{L_1}/z_{L_2} < 0$. Third, the non-symmetric nature of the interactions (condition *(iii)*) is realized by choosing beam one thicker than beam two, and setting $z_{L_1} < z_{L_2} < z_{R_2}$. Guided by these considerations, and iterative adjustments of x_{L_i} and x_{R_i} to finetune the switching thresholds, we select metamaterial parameters that meet the target ordering (figure 4(d); see appendix B).

To demonstrate that this metamaterial exhibits the three target orbits, it is initialized in the appropriate initial state and its evolution is followed during cyclic sweeps of ε between $\varepsilon_m = 0.0125$ and ε_M^5, ε_M^6 and ε_M^7 (figure 4(e)–(g)). First, for the largest driving ($k = 7$), the metamaterial exhibits a transient of two and then locks in period-two orbit where both togglerons toggle each driving cycle $(lr) \to (rl) \to (lr) \to \ldots$ (figure 4(c); see movie 2). Second, for intermediate driving ($k = 6$), the metamaterial exhibits the longest possible orbit of period $T = 4$ (figure 4(d); see movie 3). Finally, pushing the limit of our experiment, when ε_M is chosen in the narrow interval corresponding to $k = 5$, the metamaterial exhibits a short $\tau = 1$ transient and then a period three response (figure 4(e); see movie 4). Hence, a *single* metamaterial exhibits all three target orbits.

3. Conclusion and outlook

We introduced togglerons, elements which under cyclic driving repeatedly evolve over two driving cycles, as a natural step in a hierarchy of elements that starts with binary spins and hysterons. Their intrinsic multiperiodic nature facilitates the construction of complex orbits with long transients or large periods with few togglerons—features that require much larger assemblies of interacting spins or hysterons [39, 53]. As such, togglerons provide a compact and controllable route to encode rich sequential responses, opening avenues in sequential mechanisms, soft robotics and mechanical information processing [15, 16, 28, 29, 42]. Aggregate structures composed of togglerons further expand this design space and offer new routes to sequential or cyclic shape-morphing materials with potential applications ranging from complex gaits in soft-robots to *in-materia computing* [16, 20, 21, 24, 42, 47].

More broadly, in the context of amorphous and disordered systems, our work suggests that large periods and extended transients may arise from interactions between local clusters of particles which, in isolation, exhibit only short periods or transients [33–41]. This perspective provides a concrete mechanism by which complex memory effects may arise from comparatively simple microscopic constituents [17].

In extended or interacting networks of togglerons, multiple memories as well as nontrivial input sequence dependent responses could arise [17, 32]. The readout protocols required to recover these memories are therefore expected to be nontrivial, as the response can depend on both the number and ordering of training cycles–e.g. distinguishing between odd and even numbers of applied cycles. How systematic readout protocols–such as nested or competing cyclic drives–interact with hierarchies of composite elements remains an important open question.

Finally, we suggest that composite building blocks such as the togglerons, or the recently identified pairs of frustrated hysterons that capture non-trivial 'latching' memories [17] are not the end of the hierarchy. In particular for hierarchically organized materials, including glasses, exciting questions arise: which composite elements are formed, which are statistically dominant, how do they interact, and how far does this hierarchy extend? Addressing these questions may provide a fresh perspective on how complex orbits emerge in driven disordered matter.

Acknowledgments

We thank M Teunisse for analyzing spin and hysteron systems, and L Kwakernaak, H Bense, and T Brandt for fruitful discussions and J Mesman and D Ursem for technical support.

Data availability statement

The data cannot be made publicly available upon publication because the cost of preparing, depositing and hosting the data would be prohibitive within the terms of this research project. The data that support the findings of this study are available upon reasonable request from the authors.

Mov. 1-Toggleron available at https://doi.org/10.1088/1367-2630/ae45c7/data1.

Mov. 2-$(\tau, T) = (2, 2)$ orbit available at https://doi.org/10.1088/1367-2630/ae45c7/data2.

Mov. 3-$(\tau, T) = (0, 4)$ orbit available at https://doi.org/10.1088/1367-2630/ae45c7/data3.
Mov. 4-$(\tau, T) = (1, 3)$ orbit available at https://doi.org/10.1088/1367-2630/ae45c7/data4.

Funding

CMM and MvH acknowledge funding from European Research Council Grant ERC-10 101 9474.

Appendix A. Hierarchy of material bits

Here, we detail how higher-rank material bits can be constructed by composing interacting material bits of lower rank. We consider three cases: *(i)* Interacting binary spins that form a hysteron; *(ii)* Interacting hysterons that form a toggleron; *(iii)* Interacting spins that form a toggleron. We consider pairwise additive interactions [17, 39, 40, 44, 45]:

$$U_i^{\pm}(S) = u_i^{\pm} - \sum_{j \neq i} c_{ij} s_j, \tag{2}$$

where $U_i^{\pm}(S)$ denotes the switching thresholds of element i in the collective state $S = (s_1 s_2 \ldots s_N)$. For the case of binary spins, $u_i^{+} = u_i^{-}$ and $U_i^{+}(S) = U_i^{-}(S) =$. The state-dependent switching thresholds are composed of the bare switching fields $u_i^{\pm}$ and the interaction term $-\sum_j c_{ij} s_j$, and we consider both symmetric ($c_{ij} = c_{ji}$) and asymmetric interactions ($c_{ij} \neq c_{ji}$).

We first show that two spins with symmetric or asymmetric interactions can form a hysteresis loop, and that this requires avalanches where multiple spins switch simultaneously. While the argument is conceptually simple, we are not aware of any prior work in which it has been explicitly presented. Hence, hysterons can be composed of two interacting spins. We then consider interacting hysterons that exhibit a multiperiodic ($T = 2$) loop, thus forming a toggleron. From numerical sampling it was know that this requires at least three hysterons, and that for symmetric interactions, four hysterons are needed [39, 44, 53]. Here we present a systematic exploration using recently developed techniques that does not rely on sampling and is able to find all possible orbits [45, 54]. We finally consider how interacting spins can form multiperiodic orbits, and explicitly construct a $T = 2$ orbit—toggleron—using six interacting spins.

A.1. Interacting spins forming a hysteron

We now explore how binary spins can exhibit hysteretic behavior similar to a hysteron. First, we note that transitions in which one spin flips can not exhibit hysteresis (this follows directly from equation (2)). However, when avalanches are taken into account, pairs of interacting spins can produce hysteretic transitions, thus effectively forming a hysteron.

For symmetric interactions, a pair of interacting spins is characterized by three parameters: the bare switching fields u_1 and u_2, and the interaction strength $c_{12} = c_{21} = c$. Without loss of generality, we assume $u_1 > u_2$, and consider four parameter regimes given by the pair of inequalities:

$$u_1 - u_2 \gtrless |c|, \tag{3}$$

$$c \gtrless 0. \tag{4}$$

We have verified that the only possible avalanches for symmetric interactions are between the states $S =$ (00) and (11). These occur when $u_1 - u_2 < |c|$ and $c > 0$ [39, 40, 44, 45]. Then, by choosing $c > u_1 - u_2$, the spin-pair switches from state $S_1 = (00)$ to $S_2 = (11)$ when U exceeds $U^{+}(00) = u_2$ or $(11) \to (00)$ when U falls below $U^{-}(11) = u_1 - c$. Hence, two spins form a hysteron with states S_1 and S_2, and bare hysteron switching fields $u_h^{+} = u_2$ and $u_h^{-} = u_1 - c$. For asymmetric interactions ($c_{12} \neq c_{21}$), a spin pair can also exhibit hysteretic avalanches between $S = (01)$ and (10), when $c_{ij} < 0$ and $|c_{21}| > u_1 - c_{12} - u_2$, and where, the spin-pair forms a hysteron with effective switching fields: $u^{+} = u_1 - c_{12}$ and $u^{-} = u_1$. Hence, there are at least two routes for pair of spins to form a hysteron.

A.2. Multiperiodic behavior with interacting hysterons

Interacting hysterons have been studied intensely in recent years using numerical sampling techniques, providing examples of $T = 2$ multiperiodic responses that thus form togglerons [39, 40, 44]. Here, we systematically explore multiperiodic orbits adopting methods from [45, 54]. We first construct, for N hysterons, all fundamental multiperiodic orbits, and then systematically check which of these are realizable. Fundamental multiperiodic orbits are repeating sequences of states connected by single hysteron flips containing multiple episodes of up or down transitions, specified by the starting state

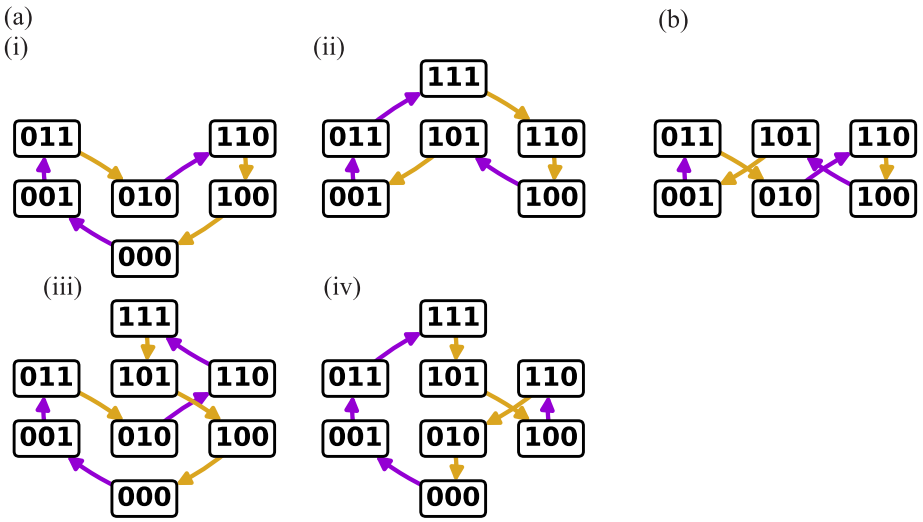

Figure 5. Realizable fundamental multiperiodic orbits with $N = 3$ hysterons and asymmetric interactions ($c_{ij} \neq c_{ji}$). (a) $T = 2$ orbits and (b) $T = 3$ orbits.

Table 1. Number of realizable multiperiodic orbits for symmetric and asymmetric interactions.

		Realizable		
N	T	$c_{ij} = c_{ji}$	$c_{ij} \neq c_{ji}$	Total
3	2	0	4	4
	3	0	1	1
4	2	62	205	205
	3	6	391	620
	4	0	76	322
	5	0	12	52

$S^0 = (s_1^0 s_2^0 \dots s_N^0)$ and the sequence of element flips $(\kappa^1, \kappa^2, \kappa^3, \dots)$ [54]. We deal with timeshift and relabeling symmetries by indexing elements according to the order in which they are flipped, and only keep orbits with initially descending order [44, 45, 54]. In addition, we order the generated multiperiodic orbits by their minimum magnetization $m := \sum_i s_i$ and filter out isomorphic orbits [54]. Together, this procedure results in a complete set of fundamental multiperiodic orbits [45, 54].

To check whether a fundamental multiperiodic orbit is realizable, we first construct a set of linear inequalities on the design parameters that needs to be satisfied to realize the orbit using pairwise interactions (equation (2)) [45]. Next, to ensure that such an orbit is traversed for cyclic driving of U between U_m and U_M, we require that the appropriate (extremal) states are both reached and stable at U_m or U_M, yielding an additional set of linear inequalities. Solvability of both sets of inequalities is easily verified, and explicit solutions can be constructed if necessary [45].

For $N = 2$ hysterons, no fundamental multiperiodic orbits exist [44]. For $N = 3$ hysterons, asymmetric interactions can produce $T = 2$ and $T = 3$ orbits [39, 44] (figure 5, table 1). Symmetric interactions require at least $N = 4$ hysterons.

A.3. Multiperiodic behavior with interacting spins

We now examine how binary spins can exhibit multiperiodic behavior similar to a toggleron. Prior numerical sampling studies have found that at least five interacting spins are required to generate period $T = 3$ orbits [14, 39]. Here, we focus on $T = 2$ behavior, and note that we are not aware (and have not been able) to create $T = 2$ orbits with five spins.

A systematic study of realizable fundamental multiperiodic orbits is not suited for spin systems, as, first, the number of orbits grows rapidly with system size, rendering exhaustive analysis impractical beyond $N > 4$ [54], and second, fundamental orbits exclude avalanches, which are essential for irreversible transitions in spin systems [45].

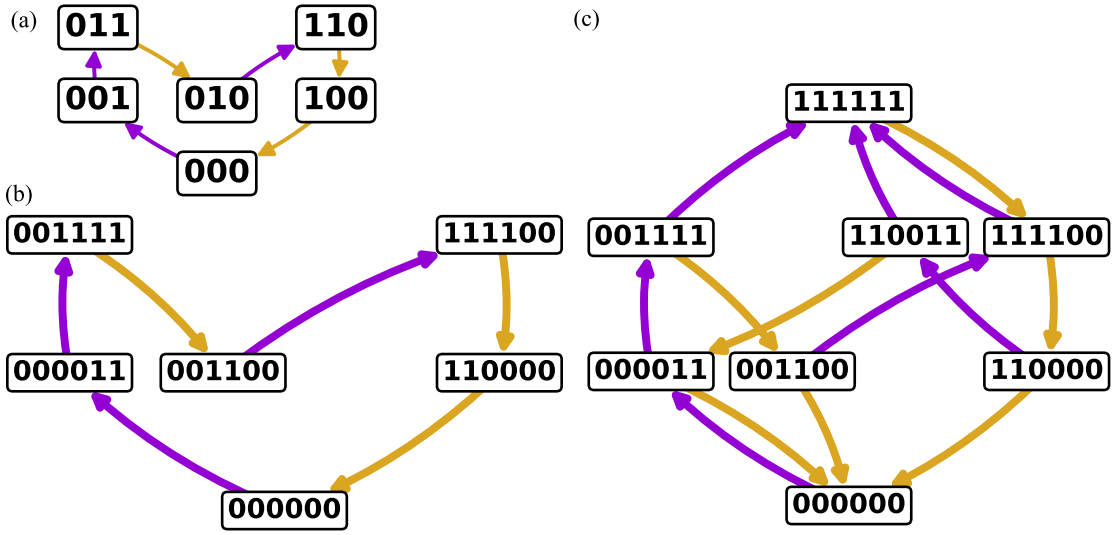

Figure 6. Construction of multiperiodic orbits in spin system. (a) Fundamental multiperiodic orbit with $T=2$, realizable with $N=3$ asymmetric interacting hysterons. (b) Resulting multiperiodic orbit with $T=2$ with $N=6$ interacting spins. (c) All transitions of the $N=6$ interacting spin system.

We construct multiperiodic orbits in spin systems by mapping spin pairs to single hysterons and using hysteron-based multiperiodic orbits. While not exhaustive, this approach offers a constructive method for generating multiperiodic behavior in systems with an even number of spins.

Our method starts with choosing a fundamental multiperiodic orbit (figure 6(a)). We generate a solution for the set of inequalities using numerical tools from [45]. The solution has bare switching fields:

$$\left(u_1^+, u_1^-\right) = (0.98, -0.49)\,, \tag{5}$$
$$\left(u_2^+, u_2^-\right) = (0.66, -1.00)\,, \tag{6}$$
$$\left(u_3^+, u_3^-\right) = (0.17, -0.92)\,, \tag{7}$$

and interaction matrix:

$$c_{ij} = \begin{pmatrix} 0 & 0.43 & -0.68 \\ -1.00 & 0 & -0.1 \\ -0.64 & -0.94 & 0 \end{pmatrix}. \tag{8}$$

For $-1.00 < U_m < -0.49$ and $0.76 < U_M < 1.23$ the orbit has $T=2$. We then map each hysteron i to a symmetrically interacting spin pair, with bare switching field of spin one $u_{1,i} = u_i^- - c$ and spin two $u_{2,i} = u_i^+$. The interactions between the spin pairs must satisfy $c_i > 0$ and $|c_i| > u_i^+ - u_i^-$. Therefore, we take $u_{1,i} = u_{2,1} + \delta$ and $c_i = u_i^+ - u_i^+ + \delta$, with $\delta = 0.01$. Furthermore, we choose to spread the interactions between each hysteron equally over the interacting spin pairs, such that each spin shifts the same amount and the same distance as the hysteron. This yields:

$$(u_{1,1}, u_{2,1}) = (0.99, 0.98)\,, \tag{9}$$
$$(u_{1,2}, u_{2,2}) = (0.67, 0.66)\,, \tag{10}$$
$$(u_{1,3}, u_{2,3}) = (0.18, 0.17)\,, \tag{11}$$

with interaction matrix (in block form):

$$c_{ij} = \begin{pmatrix} 0 & 1.48 & 0.215 & 0.215 & -0.34 & -0.34 \\ 1.48 & 0 & 0.215 & 0.215 & -0.34 & -0.34 \\ -0.50 & -0.50 & 0 & 1.67 & -0.05 & -0.05 \\ -0.50 & -0.50 & 1.67 & 0 & -0.05 & -0.05 \\ -0.32 & -0.32 & -0.47 & -0.47 & 0 & 1.10 \\ -0.32 & -0.32 & -0.47 & -0.47 & 1.10 & 0 \end{pmatrix} \tag{12}$$

Together, this produces a $T=2$ orbit (figures 6(b) and (c)).

Appendix B. Experimental details

B.1. Sample fabrication, setup and design

We now discuss the fabrication of the togglerons. Experiments are performed with beams of length $L_0 = 100 \pm 0.5\,\mathrm{mm}$, out-of-plane width of $20 \pm 0.5\,\mathrm{mm}$ and various in-plane thickness (see below). Beams are fabricated by casting two-component polyvinyl siloxane elastomer (Zhermack Elite double 22 with Young's modules 0.8 MPa and Poisson's ratio $\approx$0.5) into 3D-printed molds. After curing for seven days at room temperature, the beams are removed and dusted with talc powder to minimize friction and prevent sticking. The resulting beams exhibit predominantly elastic behavior, with minimal viscoelasticity, negligible rate-dependent effects, and no observable fatigue over repeated loading cycles.

In experiments on a single toggleron (figure 2), the lateral pushers are 3D printed and rigidly mounted on precision linear stages for accurate positioning and alignment. In the experiments on pairs of togglerons (figure 4), the lateral pushers are composed of three parts: (1) flexible legs, (2) pusher base, and (3) protrusions. The flexible legs are fabricated similarly to the beams, while the pusher base and protrusions are rigid and 3D printed. The locations x_l, x_r can be adjusted by sliding motion.

Cyclic driving is performed using a custom build compression device that allows for accurate parallel compression of wide structures (top and bottom plates remain parallel within a slope of $<0.6\,\mathrm{mm\,m^{-1}}$ [15]). The compressive strain ε is controlled by a stepper motor yielding an accuracy $\pm 0.01\,\mathrm{mm}$. During each cyclic compression protocol, a ccd camera captures the evolution of the beams at a rate of 60 Hz with $\approx 11\,\mathrm{pixels\,mm^{-1}}$. The compression speed used is $\mathrm{d}\varepsilon/\mathrm{d}t = 0.1\,\mathrm{mm\,s^{-1}}$. We note that, while we remain in the quasi-static loading regime, inertial and rate-dependent effects–such as a delayed bifurcation and inertial overshoot–can influence the snap-through behavior [48, 49, 55, 56]; a detailed quantitative treatment of these effects is left for future work.

To control the initial buckling direction of each beam, we deliberately break the symmetry by briefly contacting the beams. After contact, we wait 30 s to avoid potential viscoelastic effects induced by this interaction. Each experiment in figures 2 and 4 is repeated at least three times and we report no significant deviations.

B.2. Precise definition of phases and transitions

We now discuss how the toggleron phases, $s = l_0,\ l_1,\ r_0$, and r_1, can be detected in the real-space configuration of the beam. We consider the evolution of the toggleron shown in figure 2 of the main text. We extract the dimensional beam shape $X(Z)$ from the images, define rescaled coordinates $x = X/(L_0(1-\varepsilon))$ and $z = Z/(L_0(1-\varepsilon))$, and focus on the normalized beam shape $x(z)$. We expand the normalized shape using the first six Euler buckling modes [48]:

$$x(z) \approx \sum_{i=1}^{6} c_i \xi_i(z) \ , \tag{13}$$

where $\xi_i(z)$ is the ith mode [32, 49]. The irreversible transitions are associated to changes of the signs of the amplitudes of the first two modes; c_1 changes sign during the transition at increasing ε, and c_2 changes sign for decreasing ε (figure 7). Hence, these signs allow to extract the toggleron phase directly from the beam shape (table 2).

B.3. Design parameters

We summarize the design parameters of the two coupled togglerons presented in figure 4 of the main text. The geometry of the beams is given by $(t_{b_1}, t_{b_2}) = (4.0 \pm .1\,\mathrm{mm}, 3.0 \pm .1\,\mathrm{mm})$, and the hinge width of the flexible legs of each pusher base is $(w_{L_1}, w_{R_1}, w_{L_2}, w_{R_2}) = (2.0 \pm .1\,\mathrm{mm}, 7.0 \pm .1\,\mathrm{mm}, 2.0 \pm .1\,\mathrm{mm}, 1.8 \pm .1\,\mathrm{mm})$ (figure 8). The thickness of the flexible legs $w_p = 6.0 \pm 0.1\,\mathrm{mm}$ for all boundaries except for R_2 which is $w_p = 8.0 \pm 0.1\,\mathrm{mm}$.

Appendix C. Movie captions

Movie 1: Toggleron. Evolution of the toggleron shown in figure 2 of the main text under cyclic compression. Notice that the movie starts from zero strain and the beam first buckles upon initial compression. After this, six compression cycles are shown, before relaxing back to zero compression. Scale bar is 20 mm.

Movie 2: $(\tau, T) = (2, 2)$ orbit. Evolution of the system of two interacting togglerons for ε_M^7 (see Figure 4(e) of the main text). After initialization, six compression cycles are shown, before relaxing to zero strain. Scale bar is 20 mm.

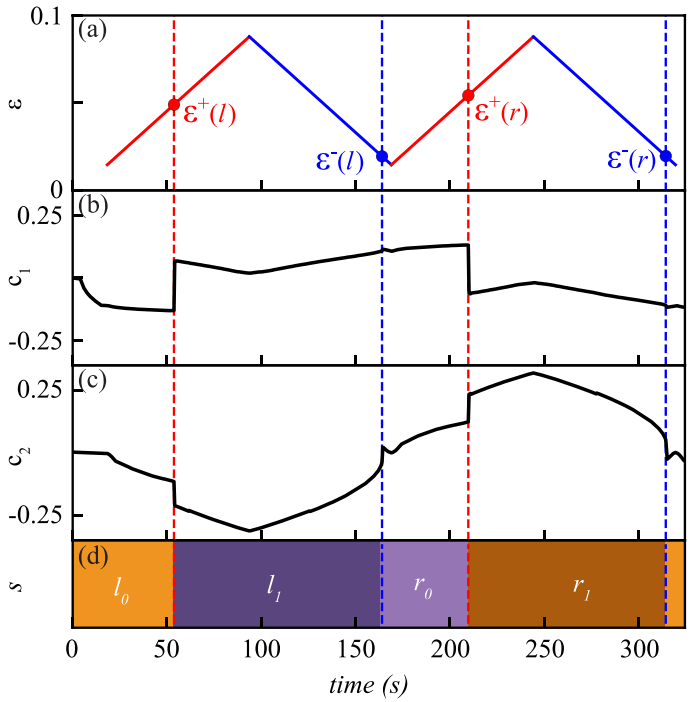

Figure 7. Modal analysis of the beam shape of the toggleron of figure 2. (a) Cyclic driving protocol with irreversible transitions during compression (red) and decompression (blue). (b)–(c) Evolution of the amplitudes of the first and second Euler modes, c_1, c_2. (d) Corresponding toggerlon phases.

Table 2. Relation between the signs of c_1 and c_2 and toggleron phase.

State	c_1	c_2
l_0	<0	$\leqslant 0$
l_1	>0	>0
r_0	>0	$\geqslant 0$
r_1	<0	<0

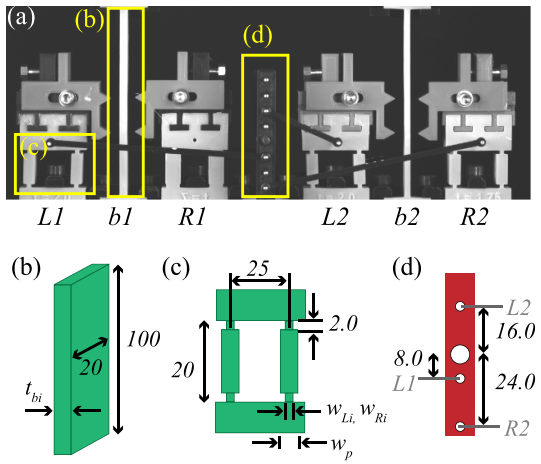

Figure 8. Geometry. (a) System indicating the left beam (b), the flexible pusher legs of boundary L_1 (c) and central pivot of the coupling mechanism (d). (b)–(d) All dimensions in mm with error 0.1 mm; in (d), gray lines denote the connection to the specified pusher.

Movie 3: $(\tau, T) = (0, 4)$ orbit. Evolution of the system of two interacting togglerons at ε_M^6 (see figure 4(f) of the main text). After initialization, 12 compression cycles are shown, before relaxing to zero strain. Scale bar is 20 mm.

Movie 4: $(\tau, T) = (1, 3)$ orbit. Evolution of the system of two interacting togglerons at ε_M^5 (see figure 4(g) of the main text). After initialization, seven compression cycles are shown, before relaxing to zero strain. Scale bar is 20 mm.

ORCID iDs

Colin M Meulblok 0009-0009-5478-4932
Martin van Hecke 0000-0002-9550-6607

References

[1] Slotterback S, Mailman M, Ronaszegi K, van Hecke M, Girvan M and Losert W 2012 Onset of irreversibility in cyclic shear of granular packings *Phys. Rev. E* **85** 021309
[2] Paulsen J D, Keim N C and Nagel S R 2014 Multiple transient memories in experiments on sheared non-brownian suspensions *Phys. Rev. Lett.* **113** 068301
[3] Adhikari M and Sastry S 2018 Memory formation in cyclically deformed amorphous solids and sphere assemblies *Eur. Phys. J. E* **41** 105
[4] Yeh W T, Ozawa M, Miyazaki K, Kawasaki T and Berthier L 2020 Glass stability changes the nature of yielding under oscillatory shear *Phys. Rev. Lett.* **124** 225502
[5] Keim N C, Hass J, Kroger B and Wieker D 2020 Global memory from local hysteresis in an amorphous solid *Phys. Rev. Res.* **2** 012004
[6] Shohat D, Hexner D and Lahini Y 2022 Memory from coupled instabilities in unfolded crumpled sheets *Proc. Natl Acad. Sci.* **119** e2200028119
[7] Bense H and van Hecke M 2021 Complex pathways and memory in compressed corrugated sheets *Proc. Natl Acad. Sci.* **118** e2111436118
[8] Paulsen J D and Keim N C 2025 Mechanical memories in solids, from disorder to design *Annu. Rev. Condens. Matter Phys.* **16** 61–81
[9] Paulsen J D and Keim N C 2019 Minimal descriptions of cyclic memories *Proc. R. Soc. A* **475** 20180874
[10] Keim N C, Paulsen J D, Zeravcic Z, Sastry S and Nagel S R 2019 Memory formation in matter *Rev. Mod. Phys.* **91** 035002
[11] Sethna J P, Dahmen K, Kartha S, Krumhansl J A, Roberts B W and Shore J D 1993 Hysteresis and hierarchies: dynamics of disorder-driven first-order phase transformations *Phys. Rev. Lett.* **70** 3347–50
[12] Deutsch J M, Dhar A and Narayan O 2004 Return to return point memory *Phys. Rev. Lett.* **92** 227203
[13] Mungan M, Sastry S, Dahmen K and Regev I 2019 Networks and hierarchies: how amorphous materials learn to remember *Phys. Rev. Lett.* **123** 178002
[14] Deutsch J M and Narayan O 2003 Subharmonics and aperiodicity in hysteresis loops *Phys. Rev. Lett.* **91** 200601
[15] Kwakernaak L J and van Hecke M 2023 Counting and sequential information processing in mechanical metamaterials *Phys. Rev. Lett.* **130** 268204
[16] Liu J, Teunisse M, Korovin G, Vermaire I R, Jin L, Bense H and van Hecke M 2024 Controlled pathways and sequential information processing in serially coupled mechanical hysterons *Proc. Natl Acad. Sci.* **121** e2308414121
[17] Lindeman C W, Jalowiec T R and Keim N C 2025 Generalizing multiple memories from a single drive: the hysteron latch *Sci. Adv.* **11** eadr5933
[18] Regev I, Attia I, Dahmen K, Sastry S and Mungan M 2021 Topology of the energy landscape of sheared amorphous solids and the irreversibility transition *Phys. Rev. E* **103** 062614
[19] Silverberg J L, Evans A A, McLeod L, Hayward R C, Hull T, Santangelo C D and Cohen I 2014 Using origami design principles to fold reprogrammable mechanical metamaterials *Science* **345** 647–50
[20] Overvelde J T B, Kloek T, D'haen J J A and Bertoldi K 2015 Amplifying the response of soft actuators by harnessing snap-through instabilities *Proc. Natl Acad. Sci.* **112** 10863–8
[21] Gelebart A H, Jan Mulder D, Varga M, Konya A, Vantomme G, Meijer E W, Selinger R L B and Broer D J 2017 Making waves in a photoactive polymer film *Nature* **546** 632–6
[22] Celli P, McMahan C, Ramirez B, Bauhofer A, Naify C, Hofmann D, Audoly B and Daraio C 2018 Shape-morphing architected sheets with non-periodic cut patterns *Soft Matter* **14** 9744–9
[23] Coulais C, Sabbadini A, Vink F and van Hecke M 2018 Multi-step self-guided pathways for shape-changing metamaterials *Nature* **561** 512–5
[24] Melancon D, Forte A E, Kamp L M, Gorissen B and Bertoldi K 2022 Inflatable origami: Multimodal deformation via multistability *Adv. Funct. Mater.* **32** 2201891
[25] Meeussen A S and van Hecke M 2023 Multistable sheets with rewritable patterns for switchable shape-morphing *Nature* **621** 516–20
[26] Chen C, Narváez C D V M, Chang N, Jimenez C M, Dennis J M, Jaeger H M, Rowan S J and de Pablo J J 2025 Tunable shear thickening, aging and rejuvenation in suspensions of shape-memory-endowed liquid crystalline particles *Proc. Natl Acad. Sci.* **122** e2425373122
[27] Serra-Garcia M 2019 Turing-complete mechanical processor via automated nonlinear system design *Phys. Rev. E* **100** 042202
[28] Yasuda H, Buskohl P R, Gillman A, Murphey T D, Stepney S, Vaia R A and Raney J R 2021 Mechanical computing *Nature* **598** 39–48
[29] Kaspar C, Ravoo B J, van der Wiel W G, Wegner S V and Pernice W H P 2021 The rise of intelligent matter *Nature* **594** 345–55
[30] Chen T, Pauly M and Reis P M 2021 A reprogrammable mechanical metamaterial with stable memory *Nature* **589** 386–90
[31] El Helou C, Grossmann B, Tabor C E, Buskohl P R and Harne R L 2022 Mechanical integrated circuit materials *Nature* **608** 699–703
[32] Meulblok C M, Singh A, Labousse M and van Hecke M 2025 Path-dependency and emergent computing under vectorial driving (arXiv:2503.07764)
[33] Schreck C F, Hoy R S, Shattuck M D and O'Hern C S 2013 Particle-scale reversibility in athermal particulate media below jamming *Phys. Rev. E* **88** 052205

[34] Regev I, Lookman T and Reichhardt C 2013 Onset of irreversibility and chaos in amorphous solids under periodic shear *Phys. Rev. E* **88** 062401
[35] Royer J R and Chaikin P M 2015 Precisely cyclic sand: self-organization of periodically sheared frictional grains *Proc. Natl Acad. Sci.* **112** 49–53
[36] Kawasaki T and Berthier L 2016 Macroscopic yielding in jammed solids is accompanied by a nonequilibrium first-order transition in particle trajectories *Phys. Rev. E* **94** 022615
[37] Lavrentovich M O, Liu A J and Nagel S R 2017 Period proliferation in periodic states in cyclically sheared jammed solids *Phys. Rev. E* **96** 020101
[38] Nagasawa K, Miyazaki K and Kawasaki T 2019 Classification of the reversible-irreversible transitions in particle trajectories across the jamming transition point *Soft Matter* **15** 7557–66
[39] Keim N C and Paulsen J D 2021 Multiperiodic orbits from interacting soft spots in cyclically sheared amorphous solids *Sci. Adv.* **7** eabg7685
[40] Lindeman C W and Nagel S R 2021 Multiple memory formation in glassy landscapes *Sci. Adv.* **7** eabg7133
[41] Szulc A, Mungan M and Regev I 2022 Cooperative effects driving the multi-periodic dynamics of cyclically sheared amorphous solids *J. Chem. Phys.* **156** 164506
[42] Kamp L M, Zanaty M, Zareei A, Gorissen B, Wood R J and Bertoldi K 2024 Reprogrammable sequencing for physically intelligent under-actuated robots (arXiv:2409.03737)
[43] Terzi M M and Mungan M 2020 State transition graph of the preisach model and the role of return-point memory *Phys. Rev. E* **102** 012122
[44] van Hecke M 2021 Profusion of transition pathways for interacting hysterons *Phys. Rev. E* **104** 054608
[45] Teunisse M H and van Hecke M 2024 Transition graphs of interacting hysterons: structure, design, organization and statistics (arXiv:2404.11344)
[46] El Elmi A and Pasini D 2024 Tunable sequential pathways through spatial partitioning and frustration tuning in soft metamaterials *Soft Matter* **20** 1186–98
[47] ten Wolde M A and Farhadi D A 2024 Single-input state-switching building block harnessing internal instabilities *Mech. Mach. Theory* **196** 105626
[48] Meulblok C M, Bense H, Caelen M and van Hecke M 2025 Early onset of snapping of slender beams under transverse forcing *Extreme Mech. Lett.* **80** 102407
[49] Pandey A, Moulton D E, Vella D and Holmes D P 2014 Dynamics of snapping beams and jumping poppers *EPL (Europhys. Lett.)* **105** 24001
[50] Vangbo M 1998 An analytical analysis of a compressed bistable buckled beam *Sens. Actuators A* **69** 212–6
[51] Sipser M 1996 Introduction to the theory of computation *ACM SIGACT News* **27** 27–29
[52] Hopcroft J E, Motwani R and Ullman J D 2001 Introduction to automata theory, languages and computation *ACM SIGACT News* **32** 60–65
[53] Paulsen J D 2025 Mechanical hysterons with tunable interactions of general sign (arXiv:2409.07726)
[54] Baconnier P, Teunisse M H and van Hecke M 2025 Proliferation and prohibition of self-loops in ensembles of interacting binary elements (arXiv:2412.12658)
[55] Liu M, Gomez M and Vella D 2021 Delayed bifurcation in elastic snap-through instabilities *J. Mech. Phys. Solids* **151** 104386
[56] Wang Q, Giudici A, Huang W, Wang Y, Liu M, Tawfick S and Vella D 2024 Transient amplification of broken symmetry in elastic snap-through *Phys. Rev. Lett.* **132** 267201